The impact of fibre surface morphology on the effective thermal conductivity of a polymer electrolyte membrane fuel cell gas diffusion layer

S.J. Botelho, A. Bazylak*

Thermofluids for Energy and Advanced Materials (TEAM) Laboratory, Department of Mechanical Engineering and Industrial Engineering, Faculty of Applied Science and Engineering, University of Toronto, 5 King's College Road, Toronto, ON M5S 3G8, Canada

HIGHLIGHTS

- Nano-scale analysis of untreated GDL within a PEM fuel cell.
- Atomic force microscopy used to analyse surface roughness of carbon fibres.
- Analytical analysis of rough contact area and thermal contact resistance.
- Empirical formulations provide realistic inputs for thermal conductivity models.

ARTICLE INFO

ABSTRACT

In this work, the effect of fibre surface morphology on the effective thermal conductivity of the gas diffusion layer of a polymer electrolyte membrane fuel cell is presented. Atomic force microscopy was used to measure the fibre surface roughness and asperity height distributions for various fibres for Toray carbon paper. Hertzian contact mechanics was used to determine individual micro-contact areas and thermal resistances, and results were compared with the smooth cylinder approximation. The effective thermal contact resistance between rough fibres was determined using resistance network theory. The thermal contact resistance and total contact area were determined for various angles of fibre orientation and contact forces; results are presented as empirical formulations. It was found that the effective thermal contact resistance is significantly affected by fibre roughness features when compared to the smooth fibre case, which is often used in the literature. The analysis conducted provides an alternative to computationally expensive surface feature analyses by providing a tool which can be used to implement the nano-scale features of gas diffusion layer fibres into existing effective thermal conductivity models.

© 2014 Elsevier B.V. All rights reserved.

1. Introduction

Polymer Electrolyte Membrane (PEM) fuel cells are electrochemical energy conversion devices that have the potential to generate electricity with zero local greenhouse gas emissions, when fed oxygen from air and hydrogen gas. An understanding of how thermal energy transfer and generation affect cell performance and tunability is needed before PEM fuel cells can be produced for commercial products. The porous gas diffusion layer (GDL) provides the main pathways for thermal conduction out of the cell through the solid phase, consisting mainly of stacked carbon fibres. During operation, the exothermic electrochemical reactions involved in water generation, and as well as ohmic resistances caused by electrical current, form temperature gradients within the cathode of the GDL. These thermal gradients affect the cell's relative humidity, water saturation, and reaction kinetics [1], which are coupled to the overall performance of the cell. It is therefore crucial to understand how the structure of the GDL can be optimized to effectively transfer heat out of the cell.

Several thermal conductivity models exist for analysing thermal conduction within the PEM fuel cell. Lattice Boltzmann methods have been used for determining the through-plane and in-plane thermal conductivity of the GDL [2–4]. Wang et al. [2] used lattice Boltzmann methods to analyse the effective thermal conductivity of unsaturated GDLs. They found that the in-plane effective thermal conductivity increases with fibre volume fraction and fibre

* Corresponding author. Tel.: +1 416 946 5031; fax: +1 416 978 7753.
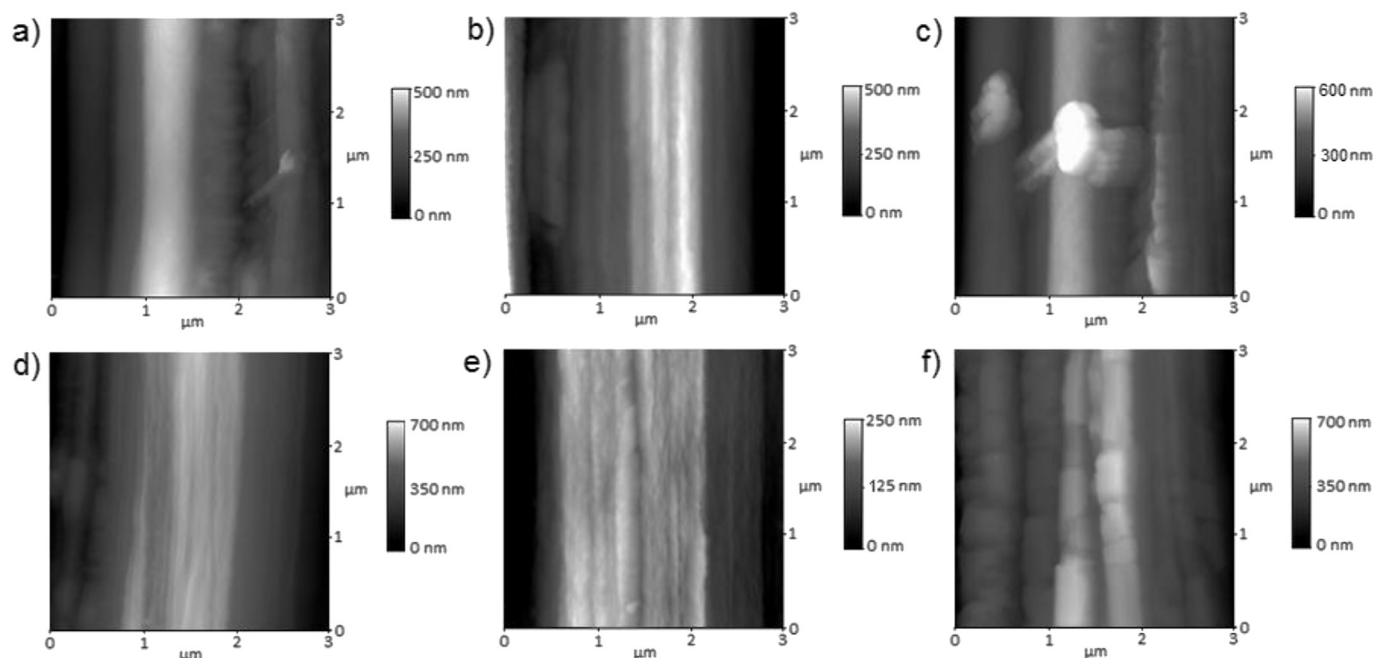E-mail address: abazylak@mie.utoronto.ca (A. Bazylak).

Fig. 1. AFM images used in rough contact analysis.

length, approaching a stable value when the fibre length becomes sufficiently long [2]. The authors also found that the through-plane effective thermal conductivity is inversely proportional to the porosity of the GDL, which was supported in lattice Boltzmann studies presented by Yablecki et al. [2,3]. Yablecki et al. [4] also determined the effect of GDL water saturation on the effective thermal conductivity. It was found that the effective thermal conductivity of the GDL increases with increasing water saturation, with a more significant effect in the through-plane direction rather than the in-plane direction [4]. Yablecki et al. [1] also used an analytical model to determine the effective thermal conductivity of compressed GDLs. Their approach was based on resistance network modelling, which was first explored by Sadeghi et al. [5,6]. It was found that the thermal resistance in the GDL is dominated by the fibre-to-fibre contacts, and the through-plane effective thermal conductivity increases linearly with GDL compression.

Although the effective thermal conductivity of the GDL has been studied, it was commonly assumed that the surfaces of the carbon fibres are smooth. In this study, the impact of incorporating realistic fibre surface morphology, in particular the circumferential fibre roughness, in effective thermal conductivity models is investigated. The results of this study could be incorporated into other existing effective thermal conductivity models, further improving their accuracy. Using an analytical approach based on Greenwood's rough contact model [7], the thermal contact resistances and contact areas between rough fibres housed in the GDL are analysed. The results obtained for various fibre orientation angles and contact forces are compared to the smooth fibre cases found in the literature and are presented with empirical formulations representing the mean and standard deviation of the contact areas and thermal contact resistances.

2. Experimental analysis

Carbon fibres housed in untreated Toray GDL were analysed using atomic force microscopy (AFM), located at the Canadian Centre for Electron Microscopy at McMaster University, Ontario. A

Nanoscope IIIa Multimode (Digital Instruments) atomic force microscope was used to image Toray TGP-H-120 carbon fibre paper without polytetrafluoroethylene (PTFE) treatment. Fibres from the top layer of the GDL were imaged to obtain the following surface feature information: roughness in the circumferential and longitudinal directions, surface area, and height deviations caused by protruding asperities or irregularities. Here it is important to note that the longitudinal roughness differs from the fibre waviness. The roughness in this context can be viewed as the deviation in the distance from the fibre surface to the central axis of the fibre in the direction considered (circumferential or longitudinal). The waviness however can be viewed as the path which the central axis of the fibre follows, where a straight central axis would correspond to a non-wavy fibre [8].

Multiple fibres were analysed, from which six sections were imaged. These sections are representative of the various types of surfaces of carbon fibres exhibited in the AFM analysis. AFM images from two locations for three fibres within untreated GDL samples are shown in Fig. 1. The six AFM images in Fig. 1 feature large and small asperities (image *b* and image *f*, respectively), protruding irregularities (image *a* and image *c*), localized flat-zones (image *e*), and sharp peaks (image *d*). A scanning frequency of 1.001 Hz was used to obtain the images with dimensions of 3 μm by 3 μm. The image dimensions were determined by the expected size of the contact area shape based on findings from previous studies assuming smooth fibre contact [1,6]; the contact area does not exceed this boundary for the forces and orientation angles

Table 1
AFM image surface feature data.

AFM image	RMS roughness [nm]	Surface area [μm²]
a	64.794	10.322
b	50.782	10.427
c	95.808	11.895
d	53.864	10.639
e	23.361	9.807
f	75.411	11.443
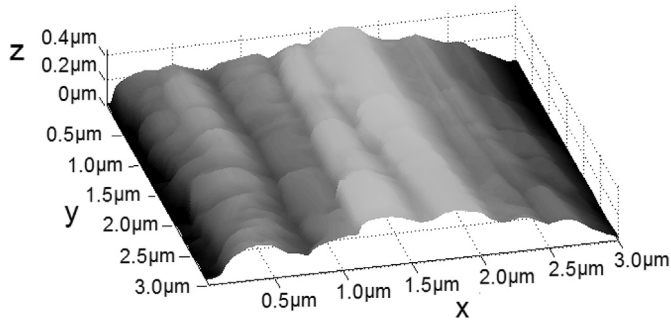
Fig. 2. 3D mapping of fibre surface data obtained using AFM for image *f*.

Table 2
Properties of the GDL carbon fibres.

Average fibre diameter, d	Average fibre length, l	Thermal conductivity, k_f	Poisson's ratio, v	Young's modulus of Elasticity, E_f
7.32 μm [1]	325 μm [1]	120 Wm^{-1} K^{-1} [1]	0.3 [14]	210 GPa [14]

considered. Table 1 includes statistical information regarding the surface features for each of the AFM images from Fig. 1, including the root-mean square (RMS) roughness and surface area. Since the rough fibres are nominally cylindrical in shape, with an assumed nominal carbon fibre diameter of 7.32 μm for Toray carbon-paper GDLs [1], the roughness values in Table 1 were obtained by plane-fitting the height information to a cylindrical plane [9]. Since the AFM images display roughness about the cylindrical surface (the nominal shape of the fibre), the plane-fit represents the height deviation with respect to the nominal diameter. The plane-fit was performed in the *x*-direction of the AFM images shown in Fig. 1 for the roughness calculation, as all fibres were oriented with the cylinder axis parallel to the *y*-direction.

Using the ASCII image data, a three-dimensional mapping of the fibre surfaces were obtained using MATLAB. Fig. 2 shows an example of one of the 3D meshes, for AFM image *f* in Fig. 1. The image depicted in Fig. 2 includes the surface features of a section of an individual carbon fibre found in the GDL. In the AFM images, the *x* and *y* axes represent the spatial co-ordinate of the AFM image, while the *z* axis represents the height of the surface. There is an appreciable degree of roughness in the *x* direction (the circumferential direction of the fibre), as opposed to the *y* direction (the longitudinal direction); this was also observed in Ref. [10]. An example fibre height profile for image *a* is shown in Fig. 3. Equally spaced slices were taken through the length and width of the AFM images to obtain roughness profiles.

While the waviness of the fibres in the longitudinal direction may have an important effect on the nature of contact between the GDL fibres and flat surfaces, such as the bipolar plate [8], the focus of this work is to evaluate the fibre-to-fibre contact within the bulk region of the GDL. Nonetheless, the fibre roughness in the circumferential direction was found to be more impactful than the roughness in the longitudinal direction. For example, Fig. 3(a) and

(b) show the height profiles of various cross-sections, traversing through the AFM images in the (a) circumferential and (b) longitudinal directions for AFM image *a*. As can be seen in Fig. 3(b), the surface is relatively smooth along the fibre length, showing a single asperity deviation in height. Similar trends were found for the other cases. Throughout the various AFM images, it was found that the largest deviation in height along the longitudinal direction caused by roughness (excluding inclusions on the fibre surface) was approximately 50 nm, which is negligible considering the degree of roughness in the circumferential direction (Fig. 3(a)). Height profiles for cross-sections at different positions along the length of the fibre are shown in Fig. 3(a). The bolded curve represents the nominal diameter of the fibre [1] and was curve-fitted to each of the respective AFM images using a root-mean square approach.

3. Methodology

An analytical approach was used to determine the contact area and thermal contact resistance of rough carbon fibres. Pairs of fibre surface profiles were analysed for a range of contact forces that would be expected within the GDL of an assembled fuel cell. A range of fibre orientation angles from 15° to 90° was also considered. The mechanical and thermal properties used in the study (Table 2) were assumed to be constant in all directions.

The range of contact forces was determined using the results of a previous study, where Yablecki et al. [1] developed analytical formulations for the number of contact points between adjacent layers of fibres in compressed GDLs. These formulations were derived using micro-computed tomography data [11], yielding porosity distributions for compressed GDLs. Using the porosity distributions, this group numerically constructed GDLs based on the nominal diameter and length of fibres housed in commercial GDLs, while assuming the fibres were preferentially stacked and allowed to overlap within adjacent layers. The number of contacts between fibres in adjacent layers was then determined using the numerically reconstructed GDLs, and presented as a function of orientation angle and average layer interface porosity [1]. Using the work of [1], we were able to determine the total number of
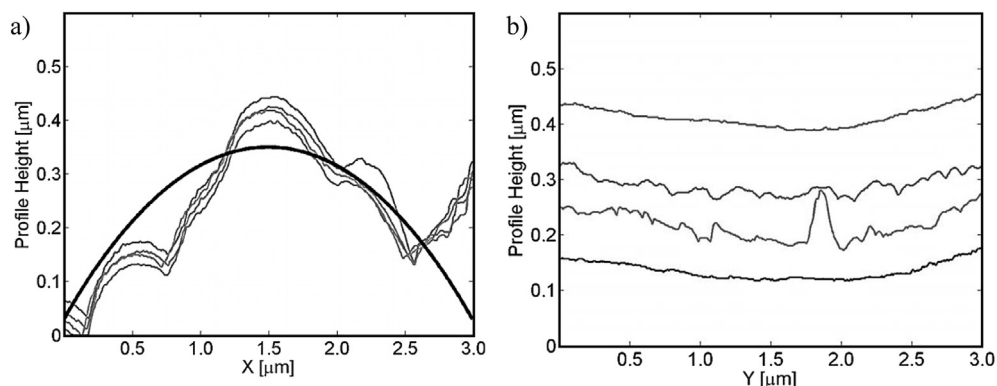

Fig. 3. Height deviation in the circumferential (a), and longitudinal (b) directions for AFM image *a*.

contact points (on average) between layers within the GDL for various GDL thicknesses. The range of contact forces experienced by the fibres in contact was then determined using the following expression:

$$F_c = (P_{GDL} l_{GDL} w_{GDL}) / C_{layer} \qquad (1)$$

where F_c is the contact force experienced between touching fibres when a GDL of length l_{GDL}, and width w_{GDL} is exposed to a through-plane pressure of P_{GDL}. Equation (1) assumes the contact force is evenly distributed amongst the number of contacts between the two layers, defined as C_{layer}. It was found that the maximum contact force occurs between the layers with largest porosity values. The largest contact force experienced between contacting fibres was calculated to be 0.01 N. Therefore, this value was used as an upper-

bound when parameterizing the contact area and thermal contact resistance with the contact force.

The focus of this study is to determine the impact of employing fibre surface morphology in the determination of effective thermal conductivity of the GDL. To that end, AFM was used to analyze the fibre surface profiles from which an analytical methodology was used to determine the contact area and thermal contact resistance. Fig. 4 shows the flowchart of the algorithm used in this study for calculating the contact area and thermal contact resistance of GDLs.

The first step in the algorithm shown in Fig. 4 is the input of the fibre contact profiles, which are different than the AFM images shown in Fig. 1. The fibre contact profiles represent analytical mappings of each asperity, comprised of a diameter and position. It was assumed that the cross-section of the fibres could be arithmetically averaged across the 3 μm length of each AFM image. The
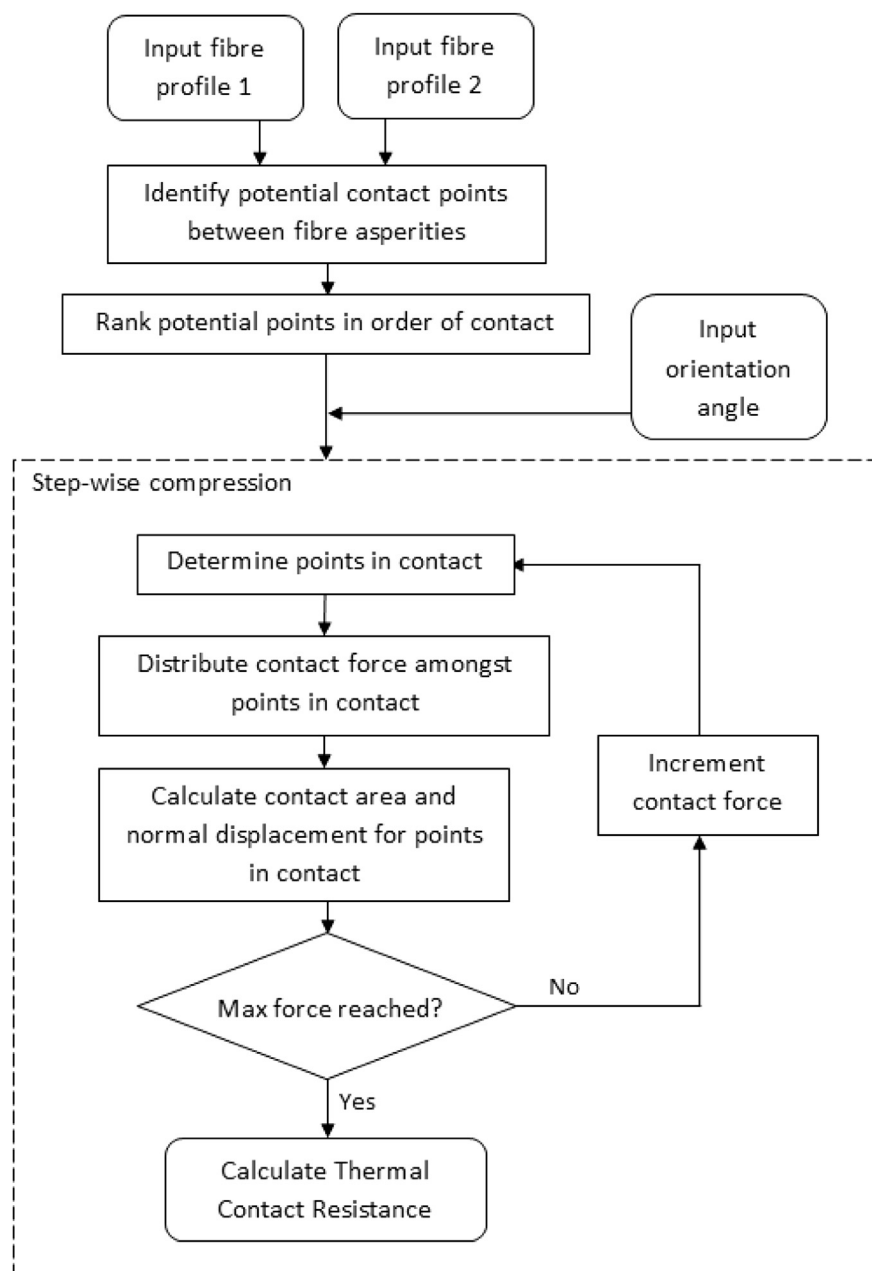

Fig. 4. Algorithm used to determine thermal contact resistance and contact area for rough contacting fibres.
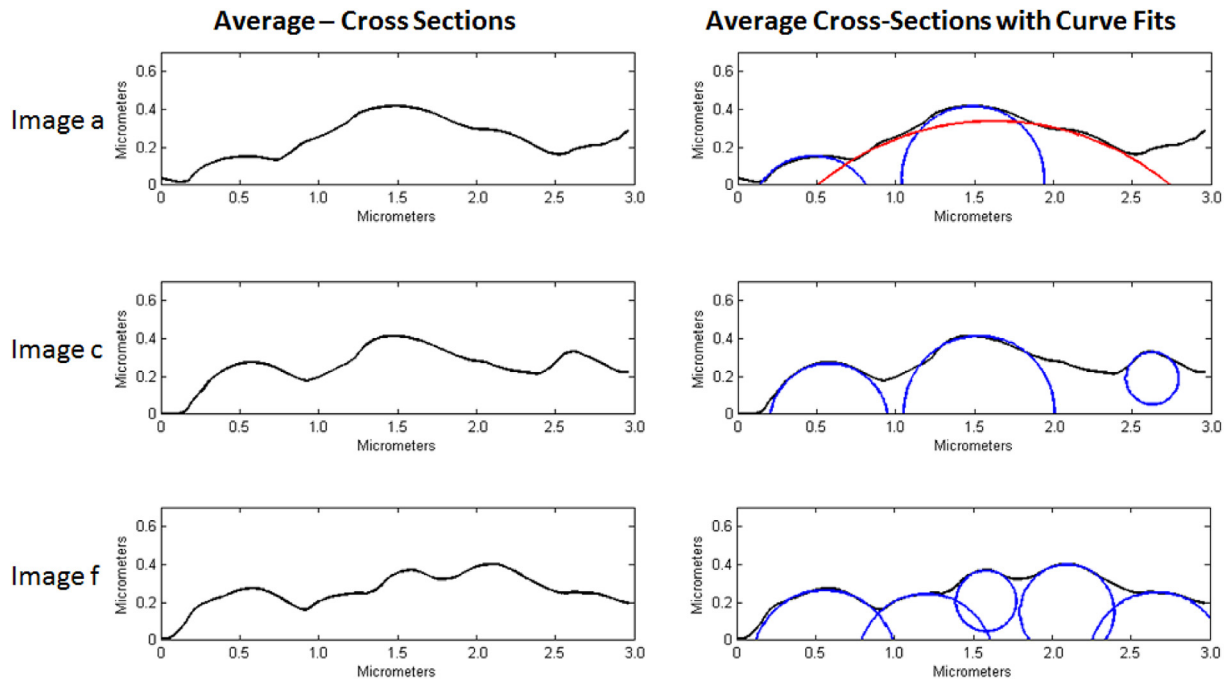
Average – Cross Sections

Average Cross-Sections with Curve Fits

Fig. 5. Average Cross-Sections with and without curve fits for AFM images *a*, *c*, and *f*.

protruding asperities were curve-fitted in each of the average cross-sections with circular curves. The diameters and heights of the circular curves were obtained using a root-mean square curve fit, as described in Ref. [9]. The assumption that the average cross-section could be used along the 3 μm length of AFM images implies that the asperities behave mechanically as small cylinders. The curve fits for three of the six AFM images from Fig. 1 are shown in Fig. 5.

Once two fibre contact profiles have been selected for analysis, the next step is to determine the number of micro-contacts. A micro-contact is formed when an asperity of one fibre comes into contact with an asperity of another fibre. The number of potential micro-contacts is the product of the number of asperities for the two fibre contact profiles considered. The red asperity curve shown for AFM image *a* is a special case, which will be described in detail in section 4.

For this study, the maximum force considered is 0.01 N, which is not large enough for the lowest asperities to come into contact with the tallest ones. Therefore, the next step in the analysis is to determine the order in which the micro-contacts potentially come into contact. For two non-parallel fibres coming into contact with an angle of orientation (θ), the order of contact is solely determined by the height of each individual asperity. In essence, the two asperities with highest peaks will come into contact first. If fibres were to be compressed together further, a second contact will be formed when one of the two initially contacting asperities meets the next tallest asperity, and so on. The distinct order of the contacts can be described as the ranking of the summed heights of all combinations of asperities for the two fibre contact profiles considered.

Once the contact problem has been fully described using the input information of the contact order, the angle of orientation is considered. In this study, an angle of orientation of 90° means the central axis of the top fibre is orthogonal to the central axis of the bottom fibre. The 0° case consisting of parallel contacting fibres is not considered in this study.

4. Contact mechanics

The method used in this study for analysing the contact of two rough fibres is based on a step-wise compression algorithm evolved from Greenwood's rough contact model [7]. Since the protruding asperities in this study are fitted with circular curves, the asperities in contact are treated as micro cylinders, rather than spherical tips as in Ref. [7]. Moreover, since there are relatively few asperities within the 3 μm by 3 μm domain, micro-contact analysis is performed individually rather than stochastically via probabilistic functions. In this study, the well-established Hertzian contact mechanics formulations are used to determine the micro-contact area and fibre normal displacement (penetration displacement). It is assumed that the individual asperities are smooth, continuous, and non-conforming surfaces, which may be compressed together while neglecting friction. The Hertzian equations are valid for small strains, which lead to stresses remaining in the elastic region for these surfaces. For the Hertzian analysis in this study, Poisson's ratio and elastic modulus are assumed constant.

The three main contact parameters considered in this study are the contact area, maximum pressure on the contact surface, and the normal displacement at the center of contact. Due to the curvature of the contacting bodies, the pressure within the contact region varies. This pressure has a maximum value where the normal displacement is maximized, i.e. the centroid of the micro-contact area, and is a maximum when the contacting fibres are orthogonal. It is important to note that if the maximum pressure exceeds the ultimate strength of 6.37 GPa for carbon fibre, the fibre will fracture [12]. Using a contact force of 0.01 N does not exceed the ultimate strength of carbon, since this force is distributed over a number of contacts.

4.1. Step- wise compression

The step-wise compression algorithm begins with the two highest asperities forming point contact. At each step, the contact

force is increased, and Hertzian analysis is used to determine the contact area and normal displacement at the locations of micro-contacts. The shapes of the micro-contacts are generally elliptical, with the shape and area being dependent on the angle of orientation and the contacting cylindrical asperity diameters. As the contact force continues to increase incrementally, a second micro-contact may form when the fibre normal displacement is sufficiently large. When more than one micro-contact occurs, the increment in contact force is distributed amongst the micro-contacts. At the instance where the second contact is formed, the asperities forming the initial micro-contact have already been compressed a certain amount. Therefore, in order to compensate for the elastic compression imposed up until this point, the increment of the contact force, rather than the total contact force, is split up evenly amongst the micro-contacts in the following iteration. In this model, it is assumed that the fibres are vertically compressed into each other (without rotation about the fibre axis).

During each step, the contact force is incremented, the algorithm determines which asperity combinations form micro-contacts, and Hertzian analysis is used to calculate the elliptical micro-contact area and normal displacement of the fibres for each micro-contact. The area of each micro-contact is calculated independently, and the effect of neighbouring asperities is assumed to be negligible in this study since the contact forces are small. However, due to the varying sizes of the asperities, there may be virtual area overlap for asperities which are in close proximity to each other. Therefore, the contact area was examined to exclude overlapping micro-contact regions.

In some cases, asperity heights have significantly lower values than the majority of asperities (*regular asperities*) found. These outliers are regarded as *macro-asperities*, an example of which is shown in Fig. 5 (red curve) (in the web version). The blue curves represent regular asperities, curve-fit to each of the protruding asperities in the average cross sections for the six AFM images. In this model, macro-asperities are utilized to handle fibre contact profiles which have asperities on top of asperities. The goal of using macro-asperities is to better approximate the contact area. For example, in AFM image *a* (Fig. 5), if the normal displacement were

to penetrate 200 nm into the fibre, the curvature of the top regular asperity (curve-fit with the blue circular curve) would poorly describe the contact area created. The model is capable of determining if the contact area should be calculated using regular asperities, or if the regular asperity should be replaced with a macro-asperity to better represent the contact scenario. When a macro-asperity is used, the initial compression of the regular asperity inside of the macro-asperity will cause higher resistance to deformation than normal.

5. Thermal analysis

Once the contact area is determined, the next step is to calculate the effective thermal contact resistance between the contacting rough fibres. The effective thermal contact resistance (*TCR*) is calculated using an equivalent resistance network representing the constriction and spreading resistances for each individual micro-contact areas. In this study, it was assumed that the only heat transfer occurring between the fibres was steady, thermal conduction through the carbon solid space. Thermal conduction along the length of the fibres was assumed to be negligible in comparison to the spreading and constriction resistances. The effect of PTFE and interstitial fluids were not considered, although the thermal conduction is mainly through the carbon as the thermal conductivity is much greater than that of other materials found in the GDL [1]. Heat transfer caused by convection was found to be negligible by Ramousse et al. [13] as the velocity of fluids through the interstitial spaces and surrounding the fibres is miniscule. Radiative heat transfer is negligible for temperatures below 1000 K [2], which is the case for PEM fuel cells operating at temperatures of approximately 80 °C (353 K). In this study, the spreading and constriction resistance values were assumed to be equivalent, which is in line with the studies conducted in Refs. [5,6,14].

Fig. 6 depicts a representation of the thermal and mechanical phenomena occurring during fibre contact [15]. The thermal energy is transferred between rough fibres through the micro-contacts. Each of the micro-contacts have their own respective spreading and constriction thermal resistances [7]. The equivalent thermal
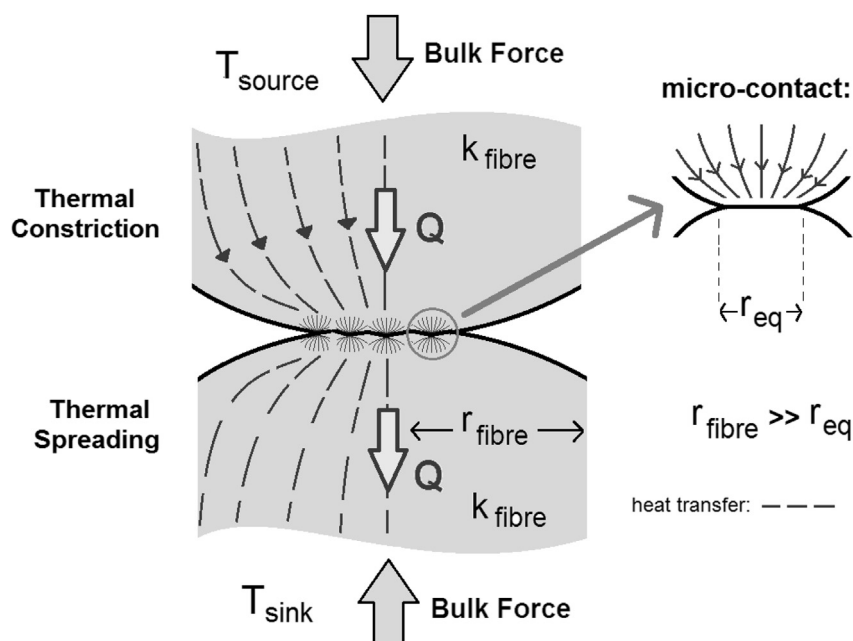

Fig. 6. Qualitative representation of heat transfer between rough fibres.

resistance network used to determine the *TCR* between two rough fibres with temperatures of T_{sink} and T_{source} is obtained by summing the constriction (R_{co}) and spreading (R_{sp}) resistances in series, then by adding the sums ($R_{co} + R_{sp}$) in parallel [7].

The formulations used to determine the thermal contact resistance for the micro-contacts are provided by Cooper et al. [16]. Here, it is assumed that the thermal domain can be treated as a flux-tube geometry considering the effect of neighbouring asperities [15]. The formulation used is presented in Equation (2), where fibre radius (r_{fibre}) is taken as 3.66 μm (half of the nominal fibre diameter), the thermal conductivity of the fibre (k_{fibre}) is
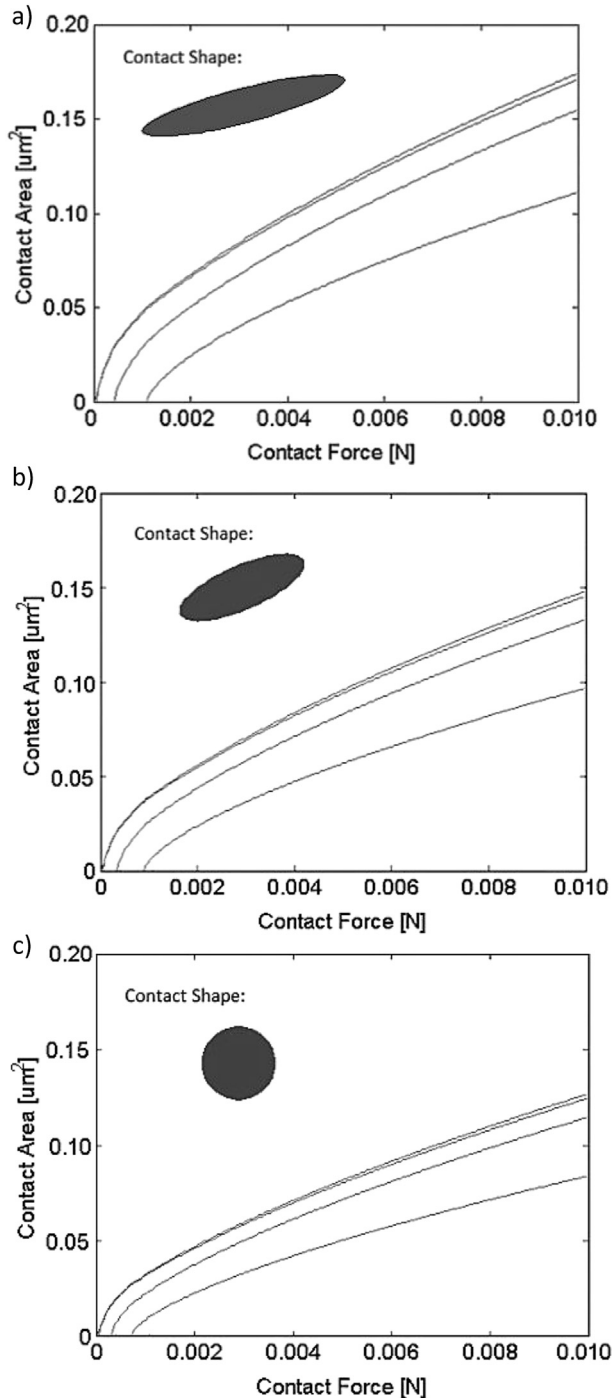
Fig. 7. Micro-contact area versus contact force for two AFM image *a* type profiles in contact, for an angle of orientation of (a) 30°, (b) 45°, and (c) 90°.
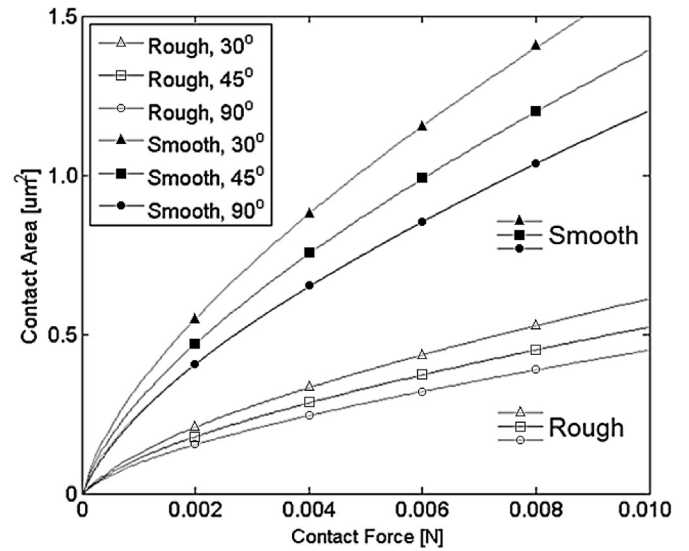
Fig. 8. Total contact area versus contact force for rough and smooth cases.
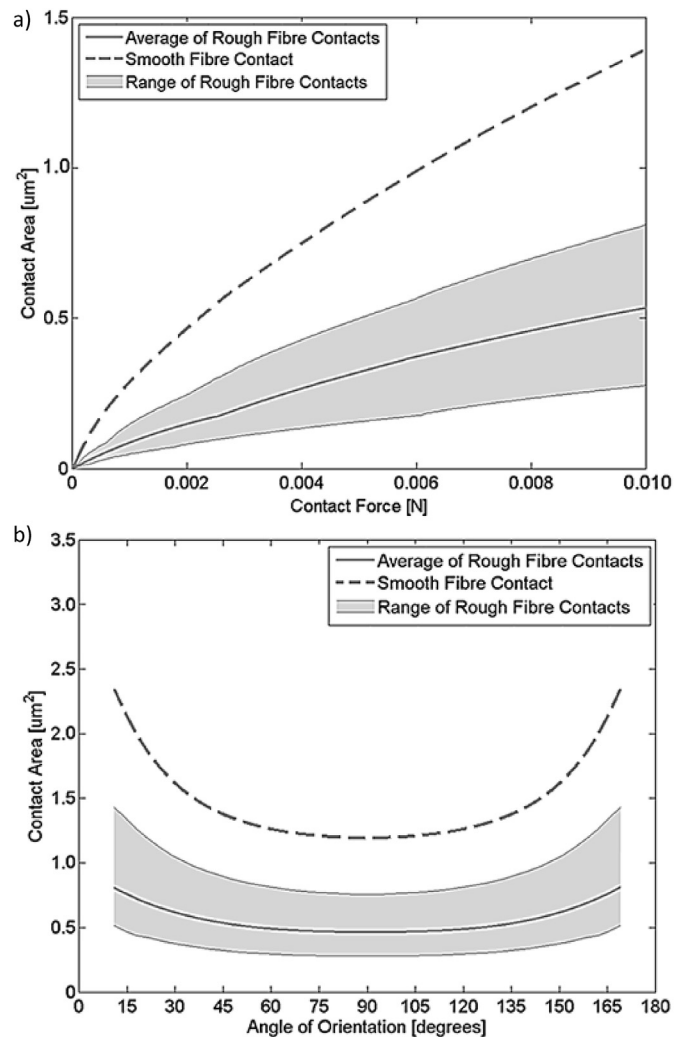
Fig. 9. Total contact area versus contact force for rough and smooth cases for an angle of orientation of 45° (a), and total contact area versus angle of orientation for rough and smooth cases for a contact force of 0.01 N (b).
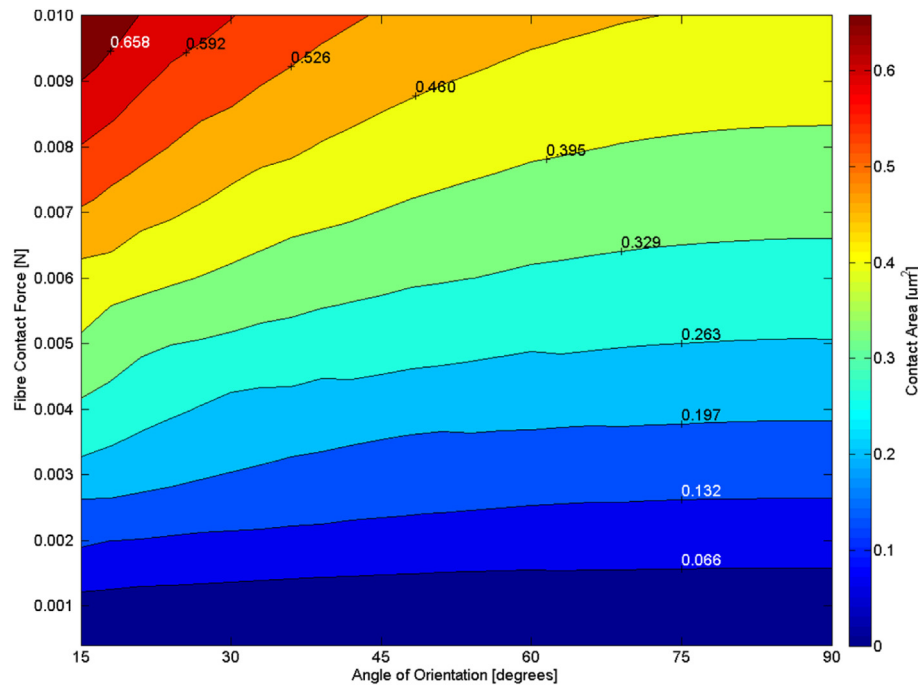
Fig. 10. Average total contact area contour plot versus angle of orientation and fibre contact force.

120 W m^{-1} K^{-1}, and the equivalent micro-contact radius (r_{eq}) is calculated using the micro-contact area: $r_{eq} = \sqrt{A_{mc}/\pi}$. Once the micro-contact areas are obtained, the thermal contact resistance per micro-contact can be calculated using Equation (2), from which the effective thermal contact resistance (*TCR*) can be computed.

$$R_{sp} = R_{co} = \left(1 - r_{eq}\big/r_{\text{fibre}}\right)^{1.5}\big/\left(2k_{\text{fibre}}r_{eq}\right) \tag{2}$$

6. Results and discussion

The following section includes the results obtained for the analyses for contact area and thermal contact resistance. The algorithm described in the previous sections is an analytical approach to determining the contact area between two rough GDL fibres. Since the surface morphology can vary between different fibres, there is a multitude of contact combinations which can occur even with only six fibre images. For example, the combinations studied in this analysis could include 256 cases formed by cross-referencing each of the AFM images, and by vertically and/or horizontally rotating fibre contact profiles prior to the analysis. Each of these cases are analysed for various angles of orientation and contact force. The sample size for this analysis is large enough to depict a wide range of fibre contact cases [10].

6.1. Contact area

Fig. 7 depicts the micro-contact area versus contact force for the case of two fibre profiles with AFM image *a* surface information

coming into contact for various angles of orientation. In these figures, each of the curves corresponds to the growth of an individual micro-contact area as the contact force is increased. For example, since profiles shown in Fig. 7 both have two asperities, having them come in contact will lead to 4 micro-contacts (four curves). In each of the three sub-figures shown in Fig. 7, some micro-contacts are formed after the initial contact. One point of interest in these figures is the change in slope of the individual contact areas. As can be seen, the rate of change of the micro-contact area with contact force decreases as new contacts are formed. The proportionality of the micro-contact area (A_{mc}) with the contact force (F_c) in Fig. 7 is $A_{mc} \propto F_c^{2/3}$, which is in line with the results of Archand [7,17,18] who defines this proportionality for contact models which assume new contacts can be formed while existing contacts continue to grow.

Fig. 7 also shows the effect of altering the orientation angle on the micro-contact area; it can be seen that the values of the micro-contact area decrease as the angle of orientation approaches 90°. When the orientation angle is 90°, there is a smaller projection of the top fibre onto the bottom fibre, resulting in smaller contact areas. When the asperities in contact have equal diameter and mechanical properties (as in the case depicted in Fig. 7(c)), the micro-contact shape is circular. For angles of orientation of 30° and 45°, the micro-contact area shape is elliptical, yielding larger contact areas than the orthogonal case. The total contact area is a summation of the individual micro-contact areas. Fig. 8 includes total contact area values for the base cases depicted in Fig. 7, and as well as data for two smooth fibres in contact (with no micro-asperities). As can be seen in Fig. 8, the total contact area for the rough and smooth cases depicts a similar trend in that the total contact area (A_{total}) has a proportionality of $A_{\text{total}} \propto F_c^{2/3}$ with the contact force [7]. The total contact area for the rough cases are significantly less than the total contact area for the smooth fibre cases, with both cases having minimums at angles of orientation of 90°.

Fig. 9 shows information regarding the total contact area for rough fibres in contact versus the contact force at a constant angle of orientation of 45° (Fig. 9(a)), and versus the angle of orientation

Table 3
Coefficients matrix for empirical mean total contact area and total contact area standard deviation formulae.

f	$\beta_0 \times 10^2$	$-\beta_1 \times 10^3$	B_2	$B_3 \times 10^5$	$-\beta_4 \times 10^1$	$-\beta_5 \times 10^{-3}$
$A_{\text{total,avg}}$	3.514	3.147	89.41	3.088	3.242	1.681
$A_{\text{total,std}}$	3.585	1.974	35.47	1.817	1.378	0.912

at a constant contact force of 0.01 N (Fig. 9(b)). In these images, the dashed line represents the smooth fibre case; fibres with no asperities. The smooth fibre approximation is typically considered in existing effective thermal conductivity analyses in the literature [1,5,6,13,14,19,20] and provide a good grounds for comparison to the rough fibre cases depicted in the blue curves. The solid, dark curve represents the arithmetically calculated average total contact area amongst the various fibre contact profile combinations. The shaded region represents the range exhibited throughout the analysis, defined by the upper and lower bounds of the total contact area values. The total contact area for the average rough case *and its upper bound* are less than the total contact area of smooth fibres in contact. This is observed for the range of angles of orientation and contact forces. The difference in the total contact area for the rough and smooth cases increases with increasing contact force, while the difference is minimal when the angle of orientation is 90°. The smooth fibre analysis can be repeated using Hertzian mechanics and the properties of the fibres provided in Table 2.

The total contact area is depicted in a contour graph as a function of angle of orientation and the contact force in Fig. 10. The data displayed in Fig. 10 is the average contact area amongst the various fibre surface profile contact combinations for various angles of orientation and contact force. As can be seen, the contact area increases with contact force, and decreases with angle of orientation (approaching the orthogonal case of 90°). The change in contact area with angle of orientation is more evident for larger contact forces. The average measured rough contact area data, shown in Fig. 10, was surface-fit to obtain an empirical formulation as a function of angle of orientation (θ) and contact force (F_c). The form of the empirical average contact area surface-fit ($A_{\text{total, avg}}$), measured in μm^2, is displayed in Equation (3).

$$f(\theta, F_c) = \beta_0 + \beta_1\theta + \beta_2 F_c + \beta_3\theta^2 + \beta_4\theta F_c + \beta_5 F_c^2 \qquad (3)$$

Since there were many different rough fibre contact combinations considered in this study, the standard deviation of the measured contact area data for each individual case was also calculated (though not included in contour form). The form of the calculated standard deviation in contact area ($A_{\text{total, std}}$) is also described in Equation (3). The constants for these two different functions are found in Table 3. The surface fits were determined using a least squares fit (MATLAB 2011a), and were fitted to the data within 98% accuracy. The surface-fits for the average contact area and contact area standard deviation are valid for the angle of orientation range considered (15°−90°), and contact force range of 0.0001 N−0.01 N. Note, the units for the input variables θ and F_c are degrees and newtons (N) respectively. The formulations shown in Equation (3) and Table 3 may serve use to those interested in incorporating fibre surface morphology between rough carbon fibres within the ranges considered. Also, these formulations could be used as an input into existing effective thermal conductivity models to incorporate surface feature information with respect to the carbon fibres. This data would be particularly useful for effective thermal conductivity models considering the effect of PTFE, binder, or interstitial fluid at the contact of rough fibres within the GDL. Users would be able to scale the amount of heat transfer conducting through the solid carbon, modifying their TCR to include the surface feature analysis. Though the contact area shape would be needed to precisely determine the spreading and constriction resistances through the micro-contact areas, the total contact area values serve as a useful scaling parameter when incorporating roughness into existing effective thermal conductivity models, comprising of multiple materials located at the contact region formed between contacting GDL fibres.

6.2. Thermal contact resistance

The *TCR* data for various fibre profiles in contact as a function of contact force and angle of orientation is shown in Fig. 11(a) and (b) respectively. Similar to Fig. 9, the data in Fig. 11 represents the average rough *TCR* amongst the various fibre profile combinations, and as well as the range exhibited through these various combinations, and the analogous smooth fibre contact. As shown in Fig. 11(b), the *TCR* for the average rough fibres in contact is significantly larger than the smooth case. The range of *TCR* values is large, constituting to approximately 40% of the average rough contact *TCR* for contact forces greater than 0.008 N, increasing with decreasing contact force to a value close to 90% of the average rough contact *TCR* for contact forces below 0.002 N. Also, the lower bound approaches the smooth fibre case for an angle of orientation near 90°. The upper bound of the rough fibre *TCR* is defined by fibre profiles with smaller asperities, leading to smaller contact areas, while the lower bound is defined by fibre profiles with larger asperities in contact. The *TCR* is sensitive to the shape of the total contact area; contact areas derived from multiple smaller micro-contacts lead to thermal contact resistances which are higher than those arising from contact areas derived from larger elliptical shapes.
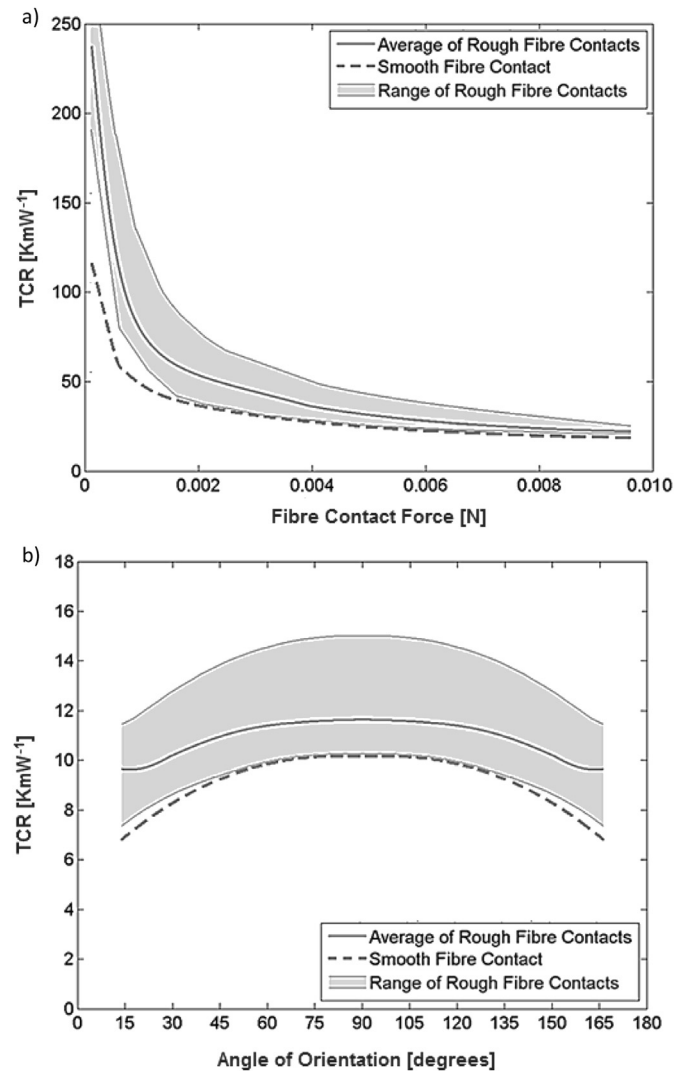

Fig. 11. Effective thermal contact resistance versus contact force for rough and smooth cases for an angle of orientation of 45° (a), and effective thermal contact resistance versus angle of orientation for rough and smooth cases for a contact force of 0.01 N (b).

Fig. 11(a) shows the effective thermal contact resistance versus the contact force. The thermal contact resistance for the rough fibre case is larger than the smooth fibre case, especially for lower contact forces. When the contact force is significantly high, the amount of compression of each of the fibres into one another becomes significantly large, and may amount to the heights of the asperities having a minimal effect on the overall *TCR*. In essence, higher contact forces cause compression area shapes that approach the smooth fibre case. The opposite is true for lower contact forces, where the surface roughness and asperity heights dominate the contact formed between rough fibres, leading to much larger *TCR* values. This is significant in the design of GDLs since there will be various contact forces experienced by fibres underneath the bipolar plates. In the regions below the bipolar plate ribs, there will be larger contact forces, and therefore, the effect of fibre surface morphology will be negligible with respect to the computed *TCR*.

A contour plot for the thermal contact resistance versus the angle of orientation and contact force is depicted in Fig. 12. The data in the contour plot is calculated similarly to that of Fig. 10, being the arithmetic average of the various fibre profile contact combinations with varying contact force and angle of orientation. The force axis is displayed in a logarithmic fashion, as there are larger gradients in thermal contact resistance for lower contact forces. The *TCR* tends to increase with increasing contact force and as the angle of orientation approaches the orthogonal case. Also, the change in *TCR* with angle of orientation is more evident for contact forces below 0.001 N; an opposite trend to that shown in the contact area contour in Fig. 10. Equation (4) shows the empirical form for the effective thermal contact resistance average values (TCR_{avg}), measured in K mW^{-1}, and the standard deviation (TCR_{std}). The standard deviation is calculated similarly to that of contact area standard deviation, $A_{total, std}$. Empirical formulations for the *TCR* were derived using MATLAB, in a similar manner to those derived for the total contact area found in Equation (3). The coefficients to the two empirical surface-fits are tabulated in Table 4, and are valid for angles of orientation of 15°–90°, and contact forces of 0.0001 N–0.01 N. The formulations shown in Equation (4) and Table 4 provide a tool used to reproduce the analysis conducted for rough fibres in contact. It is important to note that the thermal

Table 4
Coefficients matrix for empirically determined mean effective thermal contact resistance and effective thermal contact resistance standard deviation.

f	$-C_0$	$\alpha_0 \times 10^2$	α_1	$\alpha_2 \times 10^2$	$-\alpha_3 \times 10^1$	A_4
TCR_{avg}	6.211	4.197	11.9	6.606	5.08	97.42
TCR_{std}	5.307	−26.120	10.0	−2.028	3.91	58.43

contact resistance reported is solely due to the conduction through the solid space of the contact carbon asperities. Results from the *TCR* study may be validly used in analyses with other materials within the contact region (such as PTFE, binder, or interstitial fluid) causing other thermal contact resistances, though care must be taken in summing the resistance values. The analysis conducted provides an alternative to increasing the grid resolution and thus the computational costs while still considering nano-scale features within the fibre contacts.

$$f(\theta, F_c) = C_0 + \theta^{\alpha_0} + F_c^{\alpha_1} + \theta^{\alpha_2} F_c^{\alpha_3} + \exp(\alpha_4 F_c) \quad (4)$$

Future experimental validation could include the following approaches. Though outside the scope of the work presented here, the fibre-to-fibre contact resistance could be measured directly; data for which does not currently exist in the literature. Also, this model could be incorporated into a macro model, such as [4,6,21], and compared to experimentally measured bulk GDL thermal contact resistances reported by Ref. [22].

7. Conclusion

In this study, a method for determining the contact area of rough fibres in contact for various angles of orientation and contact load was presented. Fibrous surface information was obtained using atomic force microscopy for untreated Toray carbon paper TGP-H-120 GDL samples (0% PTFE content). A modification of the Greenwood rough contact model, treating the asperities as cylindrical tips (rather than the classical use of spherical surfaces), was used to determine the contact area between rough fibres. It was found that the contact area of rough fibres housed in the GDL changes with angle of orientation, with minimum values when the contacting
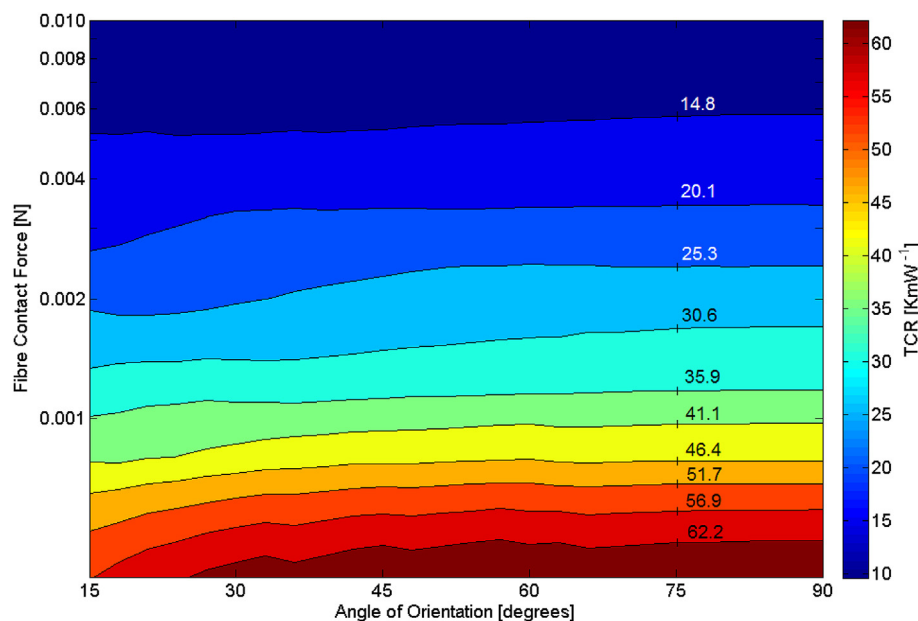

Fig. 12. Effective thermal contact resistance versus angle of orientation and fibre contact force.

fibres are orthogonal. The contact area of rough fibres was found to be less than the analogous smooth fibre case for various angles of orientation and contact force, with larger deviations for higher contact forces. The results were presented as empirical formulations which could be implemented into existing effective thermal conductivity models, providing an alternative to computation heavy analyses considering nano-scale features within the GDL fibre contacts.

It was found that the thermal contact resistance decreases with increasing contact force, with maximum points at angles of orientations of 90°. The effect of fibre surface morphology on thermal contact resistance calculations is more significant for lower contact forces, such as those imposed on fibres underneath the bipolar plate channels. Empirical formulations for the contact area and thermal contact resistance were presented, and were found to be within 98% accuracy of the average contacting fibre surface. The goal of this work was to determine the impact of the smooth-fibre assumption, and it was found that the circumferential roughness features do have a significant impact on the contact area and thermal contact resistance between fibres. The authors hope that fuel cell modellers will now incorporate these roughness features into their bulk (macro) GDL models, which should then result in more predictive thermal conductivity values that can be compared to experimental validation work.

References

[1] J. Yablecki, A. Bazylak, J. Power Sources (2012) 470–478.
[2] M. Wang, J. Wang, N. Pan, J. Phys. D Appl. Phys. 40 (1) (2007) 260–265.
[3] J. Yablecki, A. Nabovati, and A. Bazylak, 2012, Modeling the effective thermal conductivity of an anisotropic gas diffusion layer in a polymer electrolyte membrane fuel cell, 159, B647–B653.
[4] J. Yablecki, J. Hinebaugh, A. Bazylak, J. Electrochem. Soc. 159 (12) (2012) F805–F809.
[5] E. Sadeghi, N. Djilali, M. Bahrami, J. Power Sources 196 (7) (2011) 3565–3571.
[6] E. Sadeghi, N. Djilali, M. Bahrami, J. Power Sources 196 (1) (2011) 246–254.
[7] J.A. Greenwood, J.B.P. Williamson, Proc. R. Soc. Lond. 295 (1966) 300–319.
[8] H. Sadeghifar, N. Djilali, M. Bahrami, J. Power Sources (2014) 51–59.
[9] Y. Rabinovich, J. Adler, A. Ata, J. Colloid Interface Sci. 232 (1) (2000) 17–24.
[10] M. Kleinke, and M.C. Rezende, 2005, Evaluation of carbon fiber surface treated by chemical and cold plasma processes, 8(3), 281–286.
[11] Z. Fishman, J. Hinebaugh, A. Bazylak, J. Electrochem. Soc. 157 (11) (2010) B1643–B1650.
[12] S. Kim, B.K. Ahn, M.M. Mench, J. Power Sources 179 (1) (2008) 140–146.
[13] J. Ramousse, S. Didierjean, O. Lottin, Int. J. Therm. Sci. 47 (1) (2008) 1–6.
[14] E. Sadeghi, M. Bahrami, N. Djilali, J. Power Sources 179 (1) (2008) 200–208.
[15] M. Bahrami, J.R. Cullham, M.M. Yovanovich, Trans. by ASME 126 (2004) 896.
[16] M.G. Cooper, B.B. Mikic, M.M. Yovanovich, Int. J. Heat. Mass Transf. 12 (1969) 279–300.
[17] R.L. Jackson, J.L. Streator, Wear 261 (11–12) (2006) 1337–1347.
[18] B.N.J. Persson, 2006, Contact mechanics for randomly rough surfaces, 61, 201–227.
[19] J. Ramousse, O. Lottin, S. Didierjean, J. Power Sources 192 (2) (2009) 435–441.
[20] M. Wang, Q. Kang, N. Pan, Appl. Therm. Eng. 29 (2–3) (2009) 418–421.
[21] N. Zamel, X. Li, J. Shen, Chem. Eng. Sci. 65 (13) (2010) 3994–4006.
[22] O.S. Burheim, J.G. Pharoah, H. Lampert, J. Fuel Cell. Sci. Technol. 8 (2) (2011) 021013.